Chapter 7
Multicomponent Chalcogenides with Diamond-Like Structure as Thermoelectrics

Dan Zhang, Guangsheng Fu, and Shufang Wang

Abstract Due to the advantages of environment-friendly constituent elements, relatively large Seebeck coefficient, and low thermal conductivity, multicomponent diamond-like chalcogenides (MDLCs), such as $CuInTe_2$, Cu_2SnSe_3, Cu_3SbSe_4 and $Cu_2ZnSnSe_4$, have attracted intensive attention for energy conversion as promising thermoelectric (TE) materials in recent years. This chapter provides an overview of research on MDLCs in TE field. Commencing with the crystal structure and phase transition of MDLCs, we will introduce electronic structure and lattice dynamics of MDLCs through some typical TE compounds. We then discuss new methods (i.e., band engineering, entropy engineering, in situ displacement reaction, and mosaic nanostructure) developed in MDLCs for optimizing TE performance. Finally, in addition to the performance of TE device, investigations on stability and mechanical properties of MDLCs are also presented. For future practical applications of this potential material system, the problems needed to be solved and possible directions to further promote TE performance are also explored in the outlook part.

7.1 Introduction

As promising candidates to fight against energy crisis and environmental pollution, thermoelectric (TE) materials have drawn worldwide attention due to the ability to achieve direct and reversible energy conversion between heat and electricity [1–3]. The conversion efficiency of TE material is evaluated by the figure-of-merit $ZT = S^2\sigma T/\kappa$, where S is Seebeck coefficient, σ is electrical conductivity, T is absolute temperature, and κ is thermal conductivity (including electron component κ_e and lattice component κ_L). Therefore, to get high ZT, one needs large S, high σ, and low κ. However, the inherently coupled relationships among S, σ, and κ make the optimization of ZT value challenging, which means the improvement of one TE parameter is usually achieved at the cost of another [4, 5]. Recently, some effective

D. Zhang · G. Fu · S. Wang (✉)
Hebei Key Lab of Optic-Electronic Information and Materials, College of Physics Science and Technology, Hebei University, Baoding, China
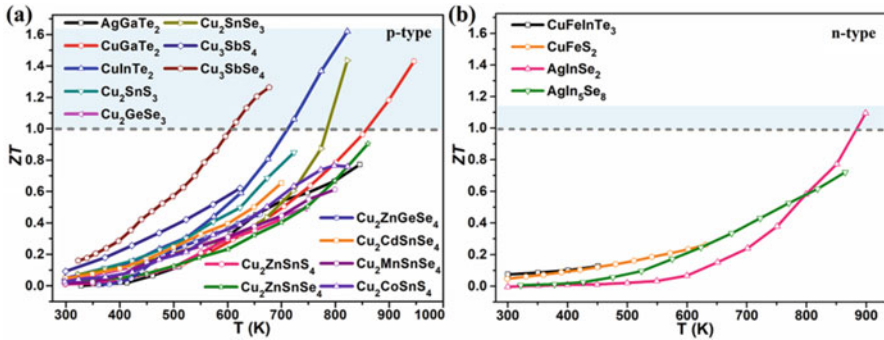e-mail: sfwang@hbu.edu.cn

Fig. 7.1 Temperature-dependent ZT of (**a**) *p*- and (**b**) *n*-type MDLC TE materials: AgGaTe$_2$ [17], CuGaTe$_2$ [18], CuInTe$_2$ [15], Cu$_2$SnS$_3$ [19], Cu$_2$GeSe$_3$ [20], Cu$_2$SnSe$_3$ [21], Cu$_3$SbS$_4$ [22], Cu$_3$SbSe$_4$ [23], Cu$_2$ZnSnS$_4$ [24], Cu$_2$ZnSnSe$_4$ [25], Cu$_2$ZnGeSe$_4$ [26], Cu$_2$CdSnSe$_4$ [27], Cu$_2$MnSnSe$_4$ [28], Cu$_2$CoSnS$_4$ [29], CuFeInTe$_3$ [30], CuFeS$_2$ [31], AgIn$_5$Se$_8$ [32], and AgInSe$_2$ [16]

strategies have been adopted to obtain high ZT values greater than 2.0 in PbTe- and SnSe-based TE materials, such as electronic density of states (DOS) distortion [6], band convergence [7] and hierarchical architectures scattering [8] in polycrystal PbTe, shifting Fermi level (E_f) close to the edge of multibands, [9] and 3D charge and 2D phonon transports in single crystal SnSe [10]. However, high toxic Pb element or cleavage fracture issue in these high-efficiency TE materials will impede the commercialization process. Hence, it is of importance to alternatively develop mechanically robust TE materials with eco-friendly and earth-abundant elements [11–14].

Multicomponent diamond-like chalcogenides (MDLCs), characterized by the diamond-like structure with deformed tetrahedron building blocks, have ZT values as high as 1.6 for *p*-type CuInTe$_2$-based [15] and 1.1 for *n*-type AgInSe$_2$-based TE materials [16] (Fig. 7.1), implying great potential for TE power generation at mid-temperature range as eco-friendly TE material [17–31]. In this chapter, crystal-line structure of MDLCs is analyzed concisely as well as the theoretical electron and phonon transport properties. Then, some new strategies to boost TE performance are discussed in MDLCs, which will provide useful reference for other TE materials. In the last part, TE device related advances in MDLCs are summarized.

7.2   Crystal Structure and Phase Transition

MDLCs and analogues (Fig. 7.2) can be viewed as derivatives from cubic zinc-blende binary II–VI compounds (e.g., ZnSe) through orderly substitution of II atoms with the same number of atoms of I + III, I$_2$ + IV, I$_3$ + V, and I$_2$ + II + IV or through other substitutions containing vacancy. Most MDLCs, such as CuInSe$_2$, Cu$_2$ZnSnSe$_4$, Cu$_3$SbSe$_4$, and AgIn$_5$Se$_8$ with cation deficiency, take in chalcopyrite

Fig. 7.2 The representative crystal structures of multicomponent diamond-like chalcogenides (MDLCs) derived from cubic zinc-blende structure
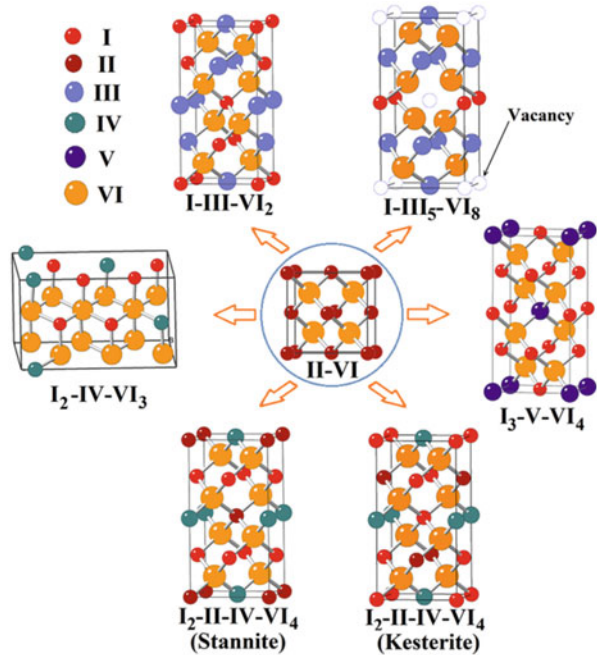
or stannite structure. But Cu_2SnSe_3-type semiconductor crystallizes in monoclinic structure with two types of anion-centered tetrahedron rather than one type of anion-centered tetrahedron in the whole structure [33]. As the substituting atoms own different ionic radius and electronegativity, the distorted lattice with diverse bonding length and angle will present in MDLCs [25, 27], which can disrupt the transport of phonons to suppress κ_L. Meanwhile, mobility of charge carriers of MDLCs will decrease also as compared with its binary counterparts. The special electron and phonon transport properties associated in compounds with diamond-like structure will be described below.

Phase transition phenomenon, which can be easily observed in some Cu- or Ag-based TE materials with non-diamond crystal structure like Cu_2Se [34], $AgBiSe_2$ [35], Cu_3SbSe_3 [36], etc., is often ignored in most MDLC TE materials. But information of temperature-dependent crystal structure is of critical significance to explain the changes of TE transport nature in different temperature ranges; therefore, it is necessary to have some general information on the phase transition of MDLCs. We focus only on some typical MDLC TE materials ($CuInTe_2$, $CuSnSe_3$, and $Cu_2ZnSnSe_4$) with phase transition in the following.

$CuInTe_2$ is I-III-VI$_2$ ternary compound and crystallizes normally in chalcopyrite structure which can be treated as a superstructure of zinc-blende type with two types of ordered cation sublattice positions. When temperature is higher than critical value T_c (~940 K), $CuInTe_2$ with ordered chalcopyrite structure will undergo a first-order phase transition and revert to zinc-blende phase with cation disorder [37]. As the disordered phase contains cross substitutions between non-isovalent cation atoms, it

exhibits electronic compensation between donor and acceptor states as well as a decrease in band gap [38]. The reported $CuGaTe_2$-, $AgInSe_2$-, and $AgInTe_2$-based TE materials also have the similar phase transition phenomenon, but this is commonly excluded from consideration in TE research because measured temperatures are obviously below T_c [37]. In addition, abnormal orthorhombic $AgInSe_2$ can be experimentally obtained under some special synthesis condition [39], and this metastable phase may be retained to normal chalcopyrite state after heating as the case in $CuInS_2$ [40].

Cu_2SnSe_3 compound is reported to own diverse crystal structures, namely, monoclinic, tetragonal, orthorhombic, and cubic [41]. The actual type of phases for Cu_2SnSe_3 at low temperatures is still controversial as different preparation conditions and compositions may lead to a variety of results. But, among mentioned phases, monoclinic is stable structure, and cubic is metastable structure which occurs at high temperature. Recently Fan et al. reported that Cu_2SnSe_3 presented in monoclinic phase at low temperature and changed to cubic zinc-blende phase with cation disorder after a phase transition at ~930 K [41]. Siyar et al. reported also that stoichiometric Cu_2SnSe_3 samples annealed at low temperatures (720–820 K) mostly possessed of monoclinic phase, while those annealed at temperature above phase transition value (960 K) were mostly of cubic phase [42]. The analogous variety in crystal structure can also be observed in Cu_2SnS_3- and Cu_2GeSe_3-based TE materials, and dimorphic or polymorphic phases can be detected simultaneously in some cases [43, 44].

As cheap and nontoxic compound Cu_2ZnSnS_4 attracts intensive research in the field of solar cell and thermoelectricity, and also its temperature-dependent change in crystal structure is explored in both theoretical and experimental aspects. It usually tends to take in kesterite structure (tetragonal) with alternating Cu/Zn and Cu/Sn planes stacked along [001] direction. As the temperature increases (Fig. 7.3a), the order-disorder transition (second-order phase transition) will take place at ~530 K, and Cu_2ZnSnS_4 will crystallize in cation-disordered kesterite structure with no change in symmetry [45]. As the further increase in temperature (Fig. 7.3b), a first-order phase transition from tetragonal-disordered kesterite to cubic zinc-blende structure will appear at ~1149 K [46].
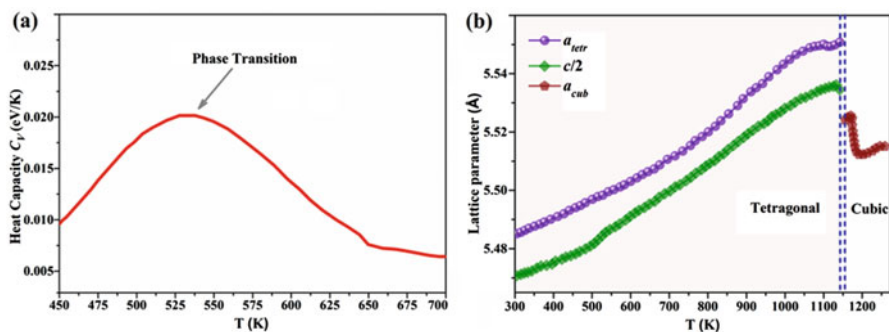

Fig. 7.3 (**a**) Temperature-dependent heat capacities and (**b**) lattice parameters of Cu_2ZnSnS_4 [45, 46]

Researchers observed also coexistence of stannite phase (which are alternatively stacked along [001] by Cu/Cu and Zn/Sn planes) in kesterite-phased Cu_2ZnSnS_4 due to small difference in enthalpies of formation between the phases [47], resulting in the variations in the band gap on the order of 100 meV [48]. However, it appears that $Cu_2GeSnSe_4$, $Cu_2ZnSnSe_4$, $Cu_2ZnSnTe_4$, etc. tend to occur in stannite structure as described in the International Centre for Diffraction Data (ICDD) of X-ray diffraction. The actual stable phase of $Cu_2ZnSnSe_4$, etc. presented at low temperature remains debatable because of the disagreements found in previous reports. On one hand, no significant difference was observed between the theoretically calculated energetic/dynamical properties of kesterite and stannite phases of either compound [49]; also, X-ray diffraction is not sensitive in distinguishing kesterite and stannite structures. On the other hand, although Cu/Zn disorder was observed by neutron diffraction or other ways [50], the deviation of stoichiometry by forming tiny second phase (like ZnSe) [51], the preserved high temperature-disordered tetragonal phase during preparation, or the existence of point defects (like $V_{Cu}^- + Zn_{Cu}^+$) in this quaternary compound [52] can also affect the reliability of results. So, most people in TE field simply treat stannite structure as ground states for most I_2-II-IV-VI_4 selenide compounds, and more detailed structural investigation and analysis are necessary as well as the mechanism for appeared phase transition in $Cu_2ZnGeSe_4$ and $Cu_2FeSnSe_4$ [26, 28].

Thus, before application in TE device, the phase transition behavior and probably related problems, for example, ionic migration, should receive utmost attention, especially in I_2-IV-VI_3 (e.g., Cu_2SnSe_3) and I_2-II-IV-VI_4 (e.g., $Cu_2ZnSnSe_4$) types of TE materials.

7.3 Electronic Structure and Lattice Dynamics of MDLCs

Analyzing electronic structure and lattice dynamic characteristics enables us to have an in-depth understanding of electron and thermal transport properties of MDLCs, thus providing insightful guidance for TE applications. In this section, electron and phonon structure of MDLCs will be simply explored by some typical chalcogenides.

Zhang et al. analyzed comparatively electronic structure of three representative diamond-like chalcogenides (ZnS, $CuGaS_2$, and Cu_2ZnSnS_4) as depicted in Fig. 7.4 and summarized main features as follows [53]. (1) Binary ZnS was a simple sp semiconductor with weak hybridization between $S - 3p$ and $Zn - 3d$ states. (2) $Cu - 3d$ orbitals in CuS_4 tetrahedron will split into t_2 and e suborbitals due to crystal field effect. In ternary $CuGaS_2$, although $Cu - 3d$-derived e states were localized, strong hybridization could occur between electrons in t_2 suborbitals and $S - 3p$ states, leading to considerable decrease in band gap as well as an increase in the slop of density of states (DOS) near valence band maximum. Thus, intrinsically large Seebeck coefficient S in most MDLC TE materials can be attributed to this relatively steep slope of DOS. (3) The conduction band minimum of Cu
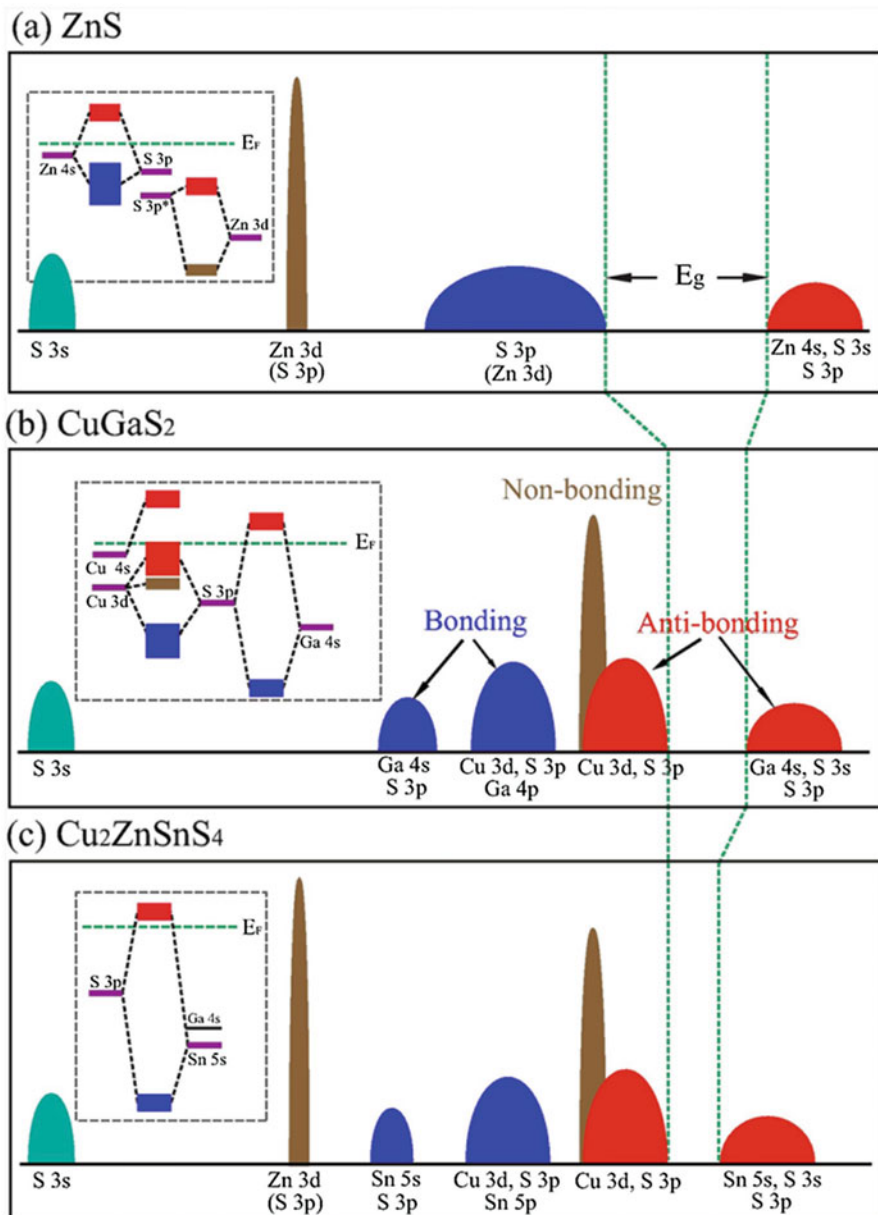
Fig. 7.4 Schematic diagram illustrating bonding for (**a**) ZnS, (**b**) CuGaS$_2$, and (**c**) Cu$_2$ZnSnS$_4$ [53]. Reproduced from Ref. [53] with permission from Elsevier

chalcogenides was primarily derived from *s* orbital of Sn (or Ga) and *p* orbitals of sulfur S, and the deeper Sn − 5*s* states of Cu$_2$ZnSnS$_4$, as compared with Ga − 4*s* orbitals of CuGaS$_2$, resulted in the further reduction of band gap. (4) The valence

band maximum of Cu chalcogenide was dominated by $p - d$ anti-bonding states, in contrast to the bonding states in ZnS.

Ab initio lattice dynamics (Fig. 7.5) of $AgInSe_2$, $CuInSe_2$ and $AgInTe_2$ were summarized by Qiu et al. [16]. (1) The acoustic phonons (heat carrying phonons) owned low sound velocity and large Grüneisen parameter γ, which are beneficial for low κ_L in crystalline compounds [54]. (2) The low-frequency optical phonons could bring resonant scattering effect and then hindered the normal transport process of acoustic phonons with similar frequencies, leading to the further decrease of κ_L [54]. (3) The discovered $Ag - Se$ "cluster vibrations" with low frequencies by phonon animation analysis explained of extremely low κ_L of $AgInSe_2$. Shao et al. reported that low κ of Cu_2GeSe_3 was related to its low Debye temperature and high bonding anharmonicity ($\gamma \sim 1.2$), based on lattice dynamic calculations [55]. Cu_3SbSe_4 compound with relatively low κ_L was reported to possess relatively large Grüneisen parameter, $\gamma(Cu_3SbSe_4) = 1.2 > \gamma(ZnSe) = 0.75$, and strong coupling between low-lying optical branches and acoustic phonon modes [56].
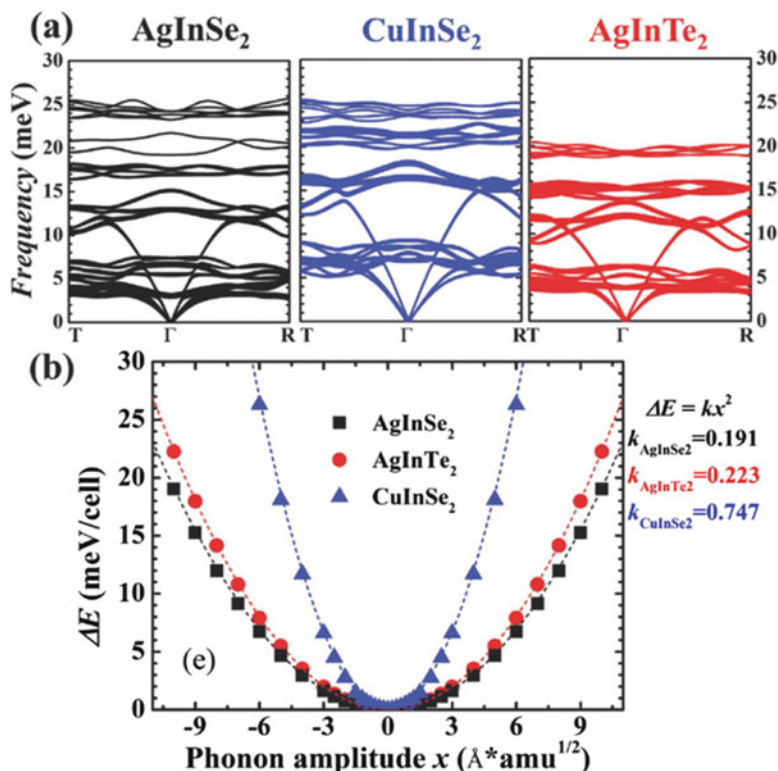

Fig. 7.5 (a) Calculated phonon spectra of $AgInSe_2$, $CuInSe_2$, and $AgInTe_2$. Line thickness denotes contributions from Ag or Cu atoms. (b) Energy difference ΔE as function of the phonon amplitude for the first optical mode caused by $Ag - Se$ (or $Cu - Se$ or $Ag - Te$) clusters [16]. Reproduced from Ref. [16] with permission from John Wiley and Sons

7.4   New Routes for High-Performance MDLC Thermoelectric Materials

In this section, we revisit only the new routes for high-performance MDLC TE materials, and other approaches, such as optimizing concentration of charge carriers and reduction of κ_L, can be found in our previous work [57].

7.4.1   Band Engineering

Pseudocubic Approach

Band convergence with increased N_v number, which is generally reported in the crystal structures with high symmetry (e.g., cubic PbTe), is desired for gaining large S without substantially degrading σ [7]. In 2014, Zhang et al. expanded this strategy into chalcopyrite with low symmetry and designed a "pseudocubic approach" (Fig. 7.6) to achieve good electronic transport properties with effective band convergence by altering the lattice toward a more cubic crystal symmetry arrangement (i.e., $\eta = \frac{c}{2a}$ toward 1) [58]. It was also verified in experiment that CuInTe$_2$ in pseudocubic structure (Cu$_{0.75}$Ag$_{0.2}$InTe$_2$ or CuIn$_{0.64}$Ga$_{0.36}$Te$_2$) possessed of significantly enhanced power factor, as well as ZT values due to band convergence
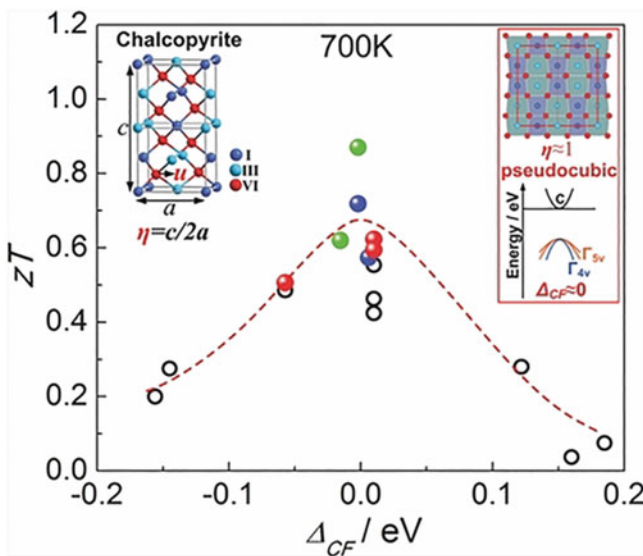

Fig. 7.6 Schematic diagram illustrating pseudocubic band convergence in ternary chalcopyrites. Symbols *c* and *a* are lattice constants. Γ_{4v} is nondegenerate band, and Γ_{5v} is double degenerate band. Δ_{CF} is the crystal field-induced energy split at top of bands Γ_{4v} and Γ_{5v}. The pseudocubic structure has cubic cation framework with Δ_{CF} embedded in noncubic distorted anion framework [58]. Reproduced from Ref. [58] with permission from John Wiley and Sons

($\Delta_{CF} \sim 0$). As reported by Zeier et al., increasing η close to unity in stannite $Cu_2ZnGeSe_4$ via Cu and Fe co-doping could increase in DOS effective mass and lead in the result to increase in power factor and ZT values, providing evidence for band convergence via crystal symmetry [59]. However, this promising approach is limited to low symmetry materials with ideal band gap and low κ_L [4].

Highly Efficient Doping (HED)

As for TE materials possessing intrinsically high band degeneracy and low concentration of charge carriers, heavy doping by guest atoms to reach the optimal concentration of charge carriers will damage more or less high band degeneracy, resulting in possible decrease of both S and power factor. Thus, selecting highly efficient dopants, which can provide optimal concentration of charge carriers at greatly lower doping content as compared with non-efficient dopants, should be a feasible attempt to improve σ while maintaining large S with little divergence of degenerate bands [60]. As exhibited in Fig. 7.7, serious separation of the degenerate bands in non-HED can be relieved by HED when the same level of high concentration of charge carriers is reached. One could clearly note the advantage of HED by Al/Ga/In compared with non-HED by Ge/Sn in high band degeneracy containing Cu_3SbSe_4: 0.5 mol. % Al/Ga/In substitution could provide comparable or even higher concentration of charge carriers as that of 1 mol. % Ge doping and also had little deviation from Pisarenko relation based on pristine Cu_3SbSe_4 due to nearly non-changed band structure. But high doping concentration (e.g., 5 mol. % Sn) made Seebeck coefficient S degrade obviously due to severe split of degenerate bands. Ultimately, ZT of samples with HED obtained is of higher value with respect to that of non-HED at 623 K.
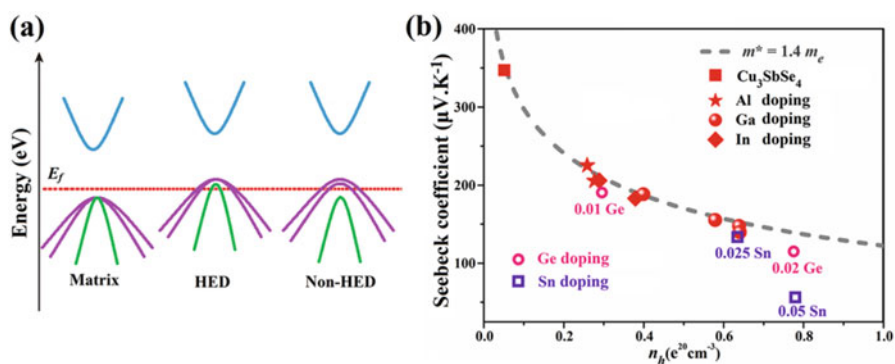

Fig. 7.7 (**a**) Schematic diagram illustrating the maintenance of highly degenerate electronic bands of matrix phase by highly efficient doping (HED). (**b**) Dependence (dashed curve) of Seebeck coefficient S on concentration of charge carriers at room temperature shows that nearly non-changed band structure is obtained via HED (i.e., Al, Ga, In doping) in Cu_3SbSe_4 with high band degeneracy [60]. Reprinted with permission from Ref. [60]. Copyright (2017) American Chemical Society

7.4.2   Entropy Engineering

Spin Entropy

It was suggested that the accompanying extra entropy in magnetic ions with degeneracy of electronic spin configurations in real space (e.g., transition metal ions with unpaired $3d$ electrons) could play an important role in getting large Seebeck coefficient S at high σ in cobalt oxides [24, 61]. This striking fact encourages many researchers to explore the possibility of substitution using magnetic ion to enhance TE performance of the other materials. Yao et al. first observed the simultaneous optimization of all three TE parameters in Mn-doped $CuInSe_2$ [62]. Mn substitution increased the concentration of charge carriers by shifting E_f downward into the region of valence band, and Mn $3d$ level hybridization with Se $4p$ level resulted in additional DOS near E_f, enabling simultaneous enhancement of σ and S for $CuInSe_2$. Introduced local disorder after Mn substitution, which was also verified by Raman spectroscopy, could contribute to the reduction of κ_L. However, the contribution of the spin entropy has been neglected by Yao et al. Up to 2013, Xiao et al. reported that magnetic ion could decouple the strongly interrelated three TE parameters in Cu_2ZnSnS_4 (Fig. 7.8) [24]. More importantly, electron paramagnetic resonance (EPR) results implied that Ni^{2+} doping truly brought extra spin into Cu_2ZnSnS_4 and, therefore, the remarkable enhancement of Seebeck coefficient S. After fully substituted with magnetic ions (e.g., Co) in Cu_2ZnSnS_4, electron and phonon structure would undergo significant change due to the strong hybridization between $3d$ states of magnetic ions and S $3p$ states, resulting in improved TE properties. Due to the distinct band structure features of Cu_2CoSnS_4 with magnetic component, high ZT ~ 0.8 could be achieved in this sulfide due to improved electron transport properties from enhanced effective mass and depressed κ_L by weakening of covalent bonding [29].
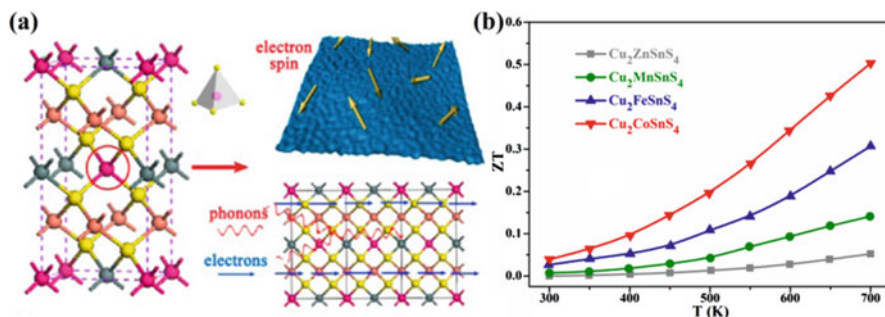

Fig. 7.8 (**a**) Schematic diagram illustrating various electron spin and phonon scatterings in quaternary magnetic sulfides. (**b**) Comparison of ZT for Cu_2XSnS_4 nanocrystals [24]. Reproduced from Ref. [24] with permission from The Royal Society of Chemistry

High-Entropy Alloys

Recently, high-entropy alloys (HEAs), which consist of multiple principal elements at equimolar or close to equimolar ratios, have been proposed as novel types of alloys with intriguing structural and functional properties [63]. Due to increased chemical complexity and configuration entropy from the occupation of multiple components at the identical atomic sites (Fig. 7.9a, b), HEA may bring significant extra phonon disorders and offer also potential way to modify band structure and result in tuning electrical and thermal transport properties [64]. HEAs of $Al_xCoCrFeNi$ ($0.0 \leq x \leq 3.0$) were firstly introduced in the context of TE by Shafeie et al. as potential and stable TE material [65]. In this scenario, Liu et al. devised a strategy of using entropy as the global gene-like performance indicator which showed how multicomponent TE materials with high configuration entropy could be designed (Fig. 7.9c, d) [64]. Firstly, parameter δ in a novel elastic model was defined by shear modulus, lattice parameters, and mismatch in the atomic radius as a criterion for judging the feasibility of forming a complete solid solution with high entropy. Guided by δ criterion, several multicomponent TE material systems were screened out. In the end, screened candidates were tested in experiment, and enhanced ZT values approached to 1.6 and 2.23 in respective $(Cu/Ag)(In/Ga)Te_2$- and $Cu_2(S/Se/Te)$-based multicomponent materials due to the optimization of entropy. Hence, entropy engineering by forming a solid solution with multiple components works as an effective guide to improve greatly TE performance through
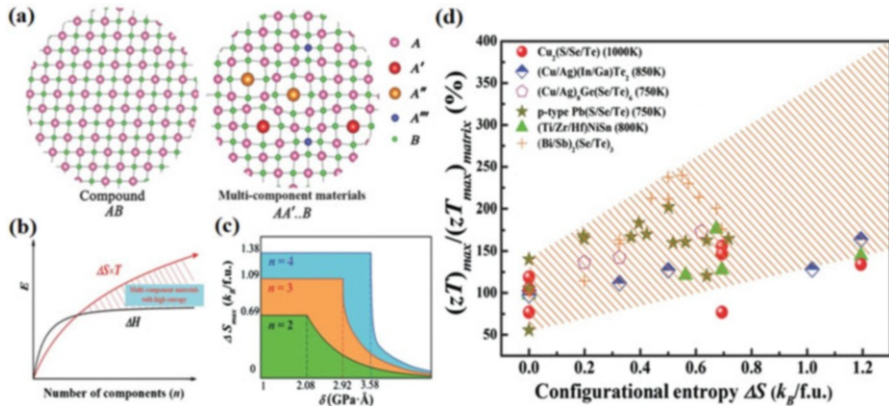

Fig. 7.9 (**a**) Schematic diagram of lattice framework in multicomponent materials compared to ordinary binary compound. (**b**) Schematic diagram of the entropy engineering with multicomponent TE materials. (**c**) The maximum configurational entropy as a function of material's solubility parameter δ for given multicomponent TE materials, where n is the number of components. (**d**) Maximum ZT as a function of configurational entropy in some multicomponent TE materials [64]. Reproduced from Ref. [64] with permission from John Wiley and Sons

the simultaneous optimization of electron and thermal transport properties, i.e., to lower κ_L by the presence of local mass and strain fluctuation and to improve S by increasing in crystal symmetry. Although this strategy holds promise for depressing κ_L, the simultaneous improvement of S is limited to some TE materials with increased crystal symmetry.

7.4.3   In Situ Displacement Reaction

In order to reduce κ_L of TE materials (e.g., skutterudite), the addition of oxide nanoinclusions is widely used to scatter phonons in nanoscale frequencies [66]. Luo et al. found firstly in situ displacement reaction between ZnO additive and $CuInTe_2$ matrix at 714 K by differential scanning calorimeter (DSC) and transmission electron microscopy (TEM) [15]. Consequently, this chemical reaction co-strengthened electron and thermal transport properties of $CuInTe_2$, i.e., to decrease in κ_L via extra phonon scattering from In_2O_3 nanoinclusions and to improve σ by formation of Zn_{In}^- point defects. Then, 80% enhanced ZT value of 1.44 had been obtained in 1 wt. % ZnO + $CuInTe_2$ sample. Furthermore, by integrating anion substitution (i.e., Sb doping) and in situ displacement reaction, high power factor of 1445 $\mu W \times m^{-1} \times K^{-2}$ and record-high ZT of 1.61 at 823 K were achieved in $CuInTe_2$-based TE material (Fig. 7.10). In addition, simultaneous optimization of electronic and thermal transport properties in TiO_2- or SnO_2-added $CuInTe_2$ illustrated also the general effectiveness of in situ displacement reaction by other oxides in enhancing TE performance [67, 68].
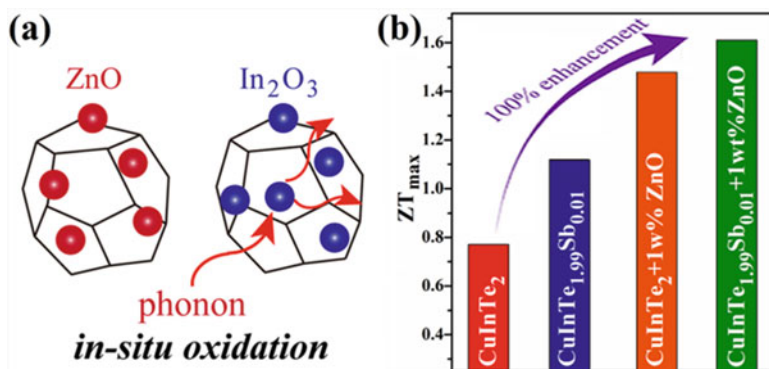

Fig. 7.10 (**a**) Schematic diagram of in situ displacement reaction. (**b**) Illustration of the stepping increment of ZT at 823 K in $CuInTe_2$ samples by Sb substitution, ZnO adding, and combined Sb substitution and ZnO adding [15]. Reproduced from Ref. [15] with permission from John Wiley and Sons

Fig. 7.11 Atomic-resolution HAADF-STEM (high-angle annular dark-field scanning transmission electron microscopy) images of mosaic nanostructures [70]. Reprinted with permission from Ref. [70]. Copyright (2018) American Chemical Society
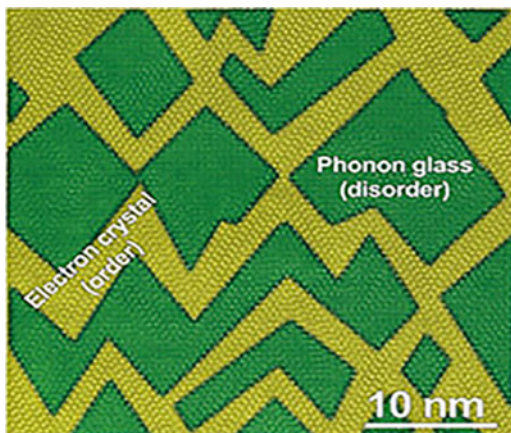
7.4.4 Mosaic Nanostructure

The strategy of nanoscale mosaic is reported to be a useful strategy to tune material's TE properties [69]. As the case in $Cu_2S_{0.5}Te_{0.5}$, high lattice coherence in mosaic crystal helps to gain excellent electron transport, whereas, the lattice strains or interfaces of mosaic nanograins are still very effective in scattering heat conducting phonons, resulting in exceptional ZT above 2 [69]. Recently, Shen et al. discovered that matrix phase of 20 mol. % Zn-doped Cu_2SnS_3 sample presented as a distinctive mosaic-type nanostructure consisting of well-defined cation-disordered domains (the "tesserae") coherently bonded to a surrounding network phase with semiordered cations (Fig. 7.11) [70]. The network phase $Cu_{4+x}Zn_{1-x}Sn_2S_7$ was found to have high mobility of charge carriers, and the tesserae had compositions closer to that of the nominal composition. More importantly, this distinctive mosaic nanostructure plays an important role in promoting TE properties due to simultaneous optimization of electron and phonon transport, i.e., charge carriers are smoothly transferred along crystalline network, while phonons are strongly scattered by atomic disorder and abrupt nanointerfaces of mosaic nanograins. Consequently, large power factor ($\sim$840 $\mu W \times m^{-1} \times K^{-2}$), ultralow κ ($\sim$0.4 $W \times m^{-1} \times K^{-1}$), and high ZT value ($\sim$0.6) at 723 K were obtained for Zn-doped Cu_2SnS_3 sample; therefore, this mosaic nanostructure represents a new type of phonon-glass electron-crystal topology, with high-mobility semiconducting phase interwoven with phonon scattering and low thermal conductivity phase.

7.5 MDLC-Based Thermoelectric Modules

Since the development of MDLC TE materials is still at the early stage, most attentions have been focused on boosting ZT; however, the feasibility to fabricate efficient TE device based on MDLCs is still an unanswered question. In this section,

we will revisit the advances in TE device of MDLCs and discuss also some device-related properties which are of critical importance in practical application.

7.5.1   Fabrication and Performance Test

In year 2017, researchers started to face this inevitable question and finally opened the door for practical applications of MDLCs TE materials. Liu et al. used firstly (Sn, Bi) co-doped nanocrystalline Cu_3SbSe_4 samples to fabricate innovative ring-shaped TE generator, and thin insulator layers were placed between rings to alter-natively contact the outer and inner rings [23]. The final assembled single p-type Cu_3SbSe_4 rings had inner and outer diameter of 28 mm and 39 mm. The test results showed that an open-circuit voltage near 20 mV was obtained for a single TE element when temperature gradient was maintained at 160 K (inner and outside ring temperatures were 250 and 90 °C, respectively) during test process. As electrical resistance of the ring <0.4 Ohm, the voltage translating into output power >1 mW for each single TE element could be obtained. Constricted by equipment setups, the actual output power density of abovementioned TE device is still unknown.

After that, the first truly TE module including both n- and p-type MDLCs had been fabricated by Qiu et al. as shown in Fig. 7.12 [16]. High-performance $Ag_{0.9}Cd_{0.1}InSe_2$ and $Cu_{0.99}In_{0.6}Ga_{0.4}Te_2$ TE materials were selected as respective n- and p-type legs to set up TE module. First, hot-pressed samples in cylinder shape were polished, diced, and electroplated in sequence. Then, obtained samples were welded to $Mo_{50}Cu_{50}$ alloy blocks with $Cu - P$ brazing filler metal at hot side and copper clad ceramic substrates with $Sn_{42}Bi_{58}$ at cold side. In order to lower the heat loss, the gap in assembled TE module with two couples was finally filled with thermal insulation material. After testing, fabricated TE module exhibited maximum output power of 0.06 W under temperature difference of 520 K. Although this output power value is still inferior to that of other well-known TE materials (e.g., PbTe) [71, 72], it opens clearly the door for applications of diamond-like TE materials.
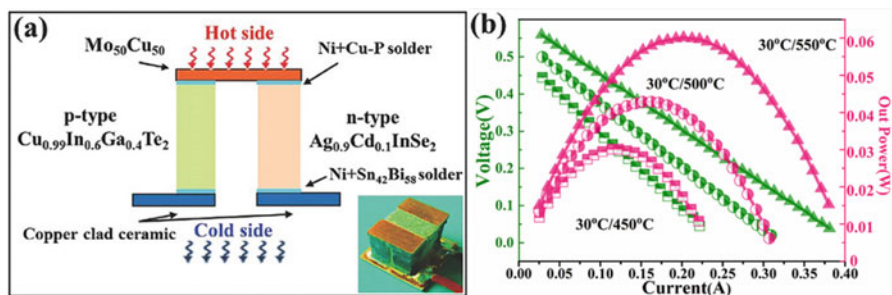

Fig. 7.12 (**a**) Schematic and photograph (inset) of fabricated diamond-like module. (**b**) Output voltage and power as function of current for TE module based on diamond-like materials [16]. Reproduced from Ref. [16] with permission from John Wiley and Sons

7.5.2 Operational Stability

Good stability with maintenance of desired TE properties upon cycling is essential to promote the widespread applications of TE materials. The issue of high-temperature instability in MDLC TE materials has attracted more and more attention in recent years. Skoug et al. reported that a dramatic decrease in both σ and ZT at high temperature was linked to physical deformation of $Cu_2Sn_{0.925}In_{0.075}(Se_{0.7}S_{0.3})_3$ sample during measurement [73]. Allowing for instability issue, the measurement of TE properties was just below 723 K in $Cu_2ZnSnSe_4$ samples despite the rising trend of ZT with temperature and high melting point (~1078 K) [74]. One could note also that variation of electronic transport properties after several high-temperature cycles was not suppressed by simply coating boron nitride layer on (Sn, Bi) co-doped Cu_3SbSe_4 sample [23]. After realizing the existence of instable properties in some MDLC TE materials, researchers start to face the problem and study it also.

In order to see temperature-dependent formation phases and crystal structure at 300–800 K of hot-pressed $CuGaTe_2$, Fujii et al. carried out synchrotron X-ray diffraction (SXRD) measurement as well as the crystal structure analysis [75]. It was revealed that Te and CuTe could precipitate from $CuGaTe_2$ matrix in temperature interval 500–650 K and this would also cause Cu and Te deficiencies in matrix phase. These impurity phases would exist in the form of liquid when temperature higher than 650 K and remained even when cooled to room temperature. Deficiencies of Cu and Te in $CuGaTe_2$ could have influence on the tetragonal distortion as well as x-coordinate of Te. Therefore, the above changes in composition as well as crystal structure will inevitably affect high-temperature stability of $CuGaTe_2$, which also can be reflected from the gradual increase in S and decrease in σ over ten measurement cycles from 300 to 800 K [76].

For the purpose of observing whether there is an occurrence of Ag-ion migration in $AgInSe_2$ compound or not, stability test was conducted by Qiu et al. [16]. The results (Fig. 7.13) showed that (1) electron transport properties were relatively reproducible during three independent cooling and heating rounds, and (2) high-temperature relative resistance (R/R_0, where R_0 is sample's initial resistance) under current density of 12 A/cm^2 was almost identical after a long time (~14 h) test, suggesting that $AgInSe_2$-based TE materials had a good stability, even under the condition of large current. To prevent oxidation, sublimation, or decomposition, a protective layer of glass sodium silicate (~1.5 mm in thickness) was coated on $Cu_{2.1}Zn_{0.9}SnSe_4$ sample, and coated sample exhibited relatively good reproducibility in electron transport properties during cooling and heating cycles [25]. In addition to protective layer, the stability can be strengthened by specific elemental doping (e.g., Ni doping in $Cu_{12}Sb_4Se_{13}$) [77] or incorporation of second phase (e.g., 3D graphene heterointerface in $Cu_{2-x}S$) [78] etc.

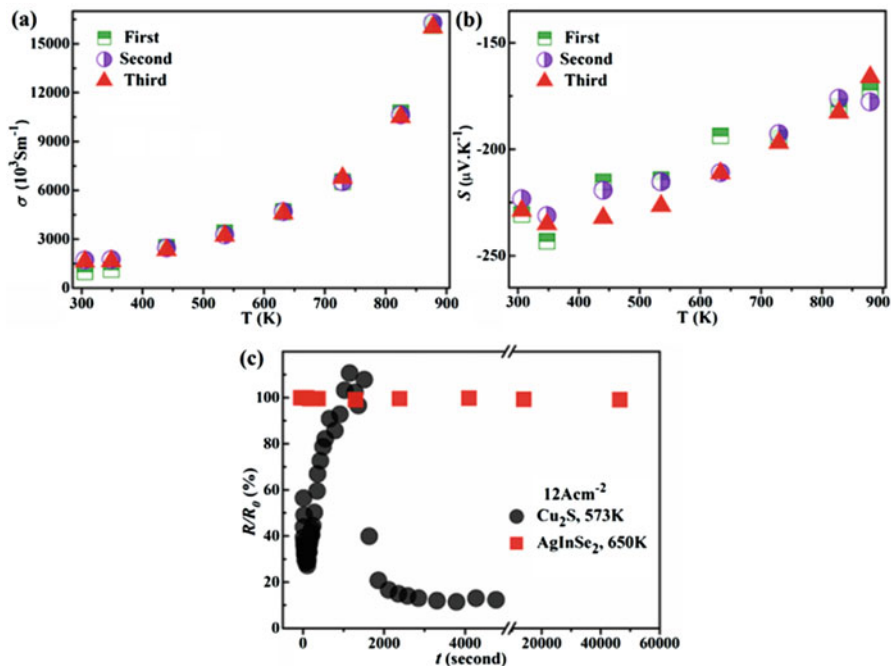**Fig. 7.13** (**a–b**) Reproducibility test for electron transport properties of $Ag_{0.9}Cd_{0.1}InSe_2$ sample. (**c**) Relative electrical resistance of $AgInSe_2$ as a function of current density of 12 A/cm^2 applied at 650 K for various time durations. The data for Cu_2S are included for comparison [16]. Reproduced from Ref. [16] with permission from John Wiley and Sons

7.5.3 Mechanical Properties

Crack or fatigue damage of TE materials, which can accelerate the deterioration of material performance as well as the failure of TE device, probably occurs because of thermomechanical stresses under temperature cycling and gradients condition [79]. So, enhancing such mechanical properties as mechanical strength and toughness is of significance for the development of MDLC TE devices.

In order to provide an insight into mechanical properties of Cu_3SbSe_4 compound, Tyagi et al. carried out hardness and fracture toughness measurements on Cu_3SbSe_4 by multimode atomic force microscope (AFM) and Vickers microhardness tester [80]. The hardness value (0.63 GPa) of Cu_3SbSe_4 compound measured by AFM agreed well with Vickers hardness value (0.65 GPa), and calculated fracture toughness was found to be 0.80 ± 0.03 MPa $\times$ m$^{1/2}$, which are comparable with those of some state-of-the-art TE materials (Fig. 7.14) mainly due to the nanoscale features in crystal size.

To understand the intrinsic mechanical properties and determine the deformation mechanism of $CuInTe_2$, Li et al. applied density functional theory (DFT) to investigate the shear deformation properties of single crystalline $CuInTe_2$ [81]. It was

Fig. 7.14 FESEM (field emission scanning electron microscopy) image of Vickers indentation cracks developed in Cu_3SbSe_4. Inset image is fracture toughness of Cu_3SbSe_4, compared with the reported values of state-of-the-art and competing TE materials [80]. Reprinted with permission from Ref. [80], with permission from AIP Publishing
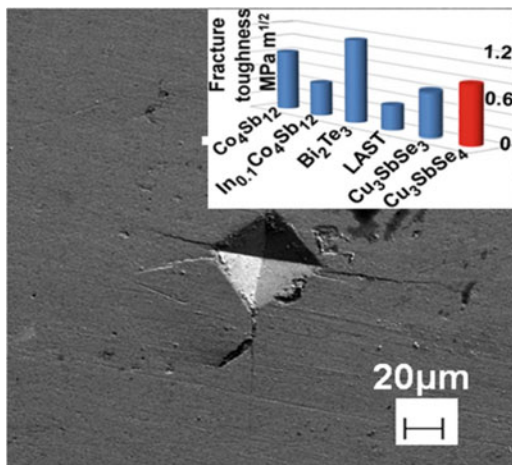
found that the lowest ideal shear strength was 2.43 GPa along (221) [11-1] slip system, which is obviously lower than those of other high-performance TE materials such as PbTe (3.46 GPa), $CoSb_3$ (7.19 GPa), and TiNiSn (10.52 GPa), suggesting that enhancing mechanical properties of $CuInTe_2$ is necessary for applications. The lowest ideal tensile strength was 4.88 GPa along [1–10] tension, and this value was higher than the lowest ideal shear strength. Moreover, the shear-induced failure arose mainly from the softening and breakage of covalent $In - Te$ bond, whereas tensile failure was arisen from breakage of $Cu - Te$ bond. The shear strength was 1.95 GPa under biaxial shear load along (221) [11-1], compression shrunk of $In - Te$ bond and resulted in buckling of $In - Te$ hexagonal framework. The fracture toughness of mode I (K_{Ic}), mode II (K_{IIc}), and mode III (K_{IIIc}) of $CuInTe_2$, which was estimated from ideal stress-strain relations, was equal to 0.19, 0.37, and 0.33 MPa $\times$ m$^{1/2}$, respectively. The fracture toughness of $CuInTe_2$ was much lower than those of ZnO, but greatly higher than that of such layered materials as $BiCuSeO$ and $NaCo_2O_4$. Additionally, relatively poor mechanical properties of $CuInTe_2$ can be strengthened through elemental substitution (e.g., S/Se doping in PbTe) [82], grain size reduction, crystal orientation regulation [83] or addition of nanosized secondary reinforcements [84], and so on.

7.6 Conclusion and Outlook

Recently, MDLCs have attracted an ever-increasing attention in TE field, and TE performance, measured in terms of ZT value, was significantly enhanced to 1.6 in 2017. The effective strategies including pseudocubic structure, highly efficient doping, spin entropy, high-entropy alloys, in situ displacement reaction, and mosaic nanostructure have been successfully utilized in improving TE properties of

MDLCs. Furthermore, diamond-like TE module with only two pairs can provide an output power of 0.06 W under a temperature difference of 520 K. Despite the major advances in ZT and device have been achieved in MDLCs with good prospects, more efforts are still needed to promote the widespread use of MDLC materials in power generation applications. First, ZT value, especially average one, cannot be as good as that of mainstream TE materials, so it is necessary to further increase in ZT by new strategies, such as dislocation engineering [85], resonant levels [86], and nanoheterostructure [87]. Second, as ZT reported in *n*-type MDLC is still inferior to that of *p*-type ones (Fig. 7.1), obtaining high-performance *n*-type MDLC is also urgently needed in future research. Third, in addition to excellent TE properties, mechanical properties, thermal stability, and choosing contact layer, which are of equal importance in commercial applications, should be also investigated intensively for MDLC materials [88]. Finally, MDLCs, not only TE material but also light absorber, probably have good application in photovoltaic-thermoelectric hybrid device if Seebeck effect and photovoltaic effect could be incorporated together in a proper way [89, 90].

References

1. L.E. Bell, Science **321**(5895), 1457–1461 (2008)
2. D. Champier, Energy Convers. Manag. **140**, 167–181 (2017)
3. S. Twaha, J. Zhu, Y. Yan, B. Li, Renew. Sust. Energ. Rev. **65**, 698–726 (2016)
4. J. He, T.M. Tritt, Science **357**(6358), eaak9997 (2017)
5. L. Yang, Z.G. Chen, M.S. Dargusch, J. Zou, Adv. Energy Mater. **8**(6), 1701797 (2018)
6. J.P. Heremans, V. Jovovic, E.S. Toberer, A. Saramat, K. Kurosaki, A. Charoenphakdee, S. Yamanaka, G.J. Snyder, Science **321**(5888), 554–557 (2008)
7. Y. Pei, X. Shi, A. LaLonde, H. Wang, L. Chen, G.J. Snyder, Nature **473**(7345), 66 (2011)
8. K. Biswas, J.Q. He, I.D. Blum, C.I. Wu, T.P. Hogan, D.N. Seidman, V.P. Dravid, M.G. Kanatzidis, Nature **489**(7416), 414 (2012)
9. L.D. Zhao, G.J. Tan, S.Q. Hao, J.Q. He, Y.L. Pei, H. Chi, H. Wang, S.K. Gong, H.B. Xu, V.P. Dravid, C. Uher, G.J. Snyder, C. Wolverton, M.G. Kanatzidis, Science **351**, 141–144 (2015)
10. C. Chang, M. Wu, D. He, Y. Pei, C.F. Wu, X. Wu, H. Yu, F. Zhu, K. Wang, Y. Chen, L. Huang, J.F. Li, J. He, L.D. Zhao, Science **360**(6390), 778–783 (2018)
11. P. Qiu, X. Shi, L. Chen, Energy Storage Materials **3**, 85–97 (2016)
12. D. Zhang, J. Yang, Q. Jiang, L. Fu, Y. Xiao, Y. Luo, Z. Zhou, J. Mater. Chem. A **4**, 4188–4193 (2016)
13. D. Zhang, J. Yang, Q. Jiang, L. Fu, Y. Xiao, Y. Luo, Z. Zhou, Mater. Design **98**, 150–154 (2016)
14. Z. Ge, L. Zhao, D. Wu, X. Liu, B. Zhang, J. Li, J. He, Mater. Today **19**(4), 227–239 (2016)
15. Y. Luo, J. Yang, Q. Jiang, W. Li, D. Zhang, Z. Zhou, Y. Cheng, Y. Ren, X. He, Adv. Energy Mater. **6**(12), 1600007 (2016)

16. P. Qiu, Y. Qin, Q. Zhang, R. Li, J. Yang, Q. Song, Y. Tang, S. Bai, X. Shi, L. Chen, Adv. Sci. **5**(3), 1700727 (2018)
17. A. Yusufu, K. Kurosaki, A. Kosuga, T. Sugahara, Y. Ohishi, H. Muta, S. Yamanaka, Appl. Phys. Lett. **99**(6), 061902 (2011)
18. T. Plirdpring, K. Kurosaki, A. Kosuga, T. Day, S. Firdosy, V. Ravi, G.J. Snyder, A. Harnwunggmoung, T. Sugahara, Y. Ohishi, H. Muta, S. Yamanaka, Adv. Mater. **24**(27), 3622–3626 (2012)
19. H. Zhao, X. Xu, C. Li, R. Tian, R. Zhang, Y. Lyu, D. Li, X. Hu, L. Pan, Y. Wang, J. Mater. Chem. A **5**(44), 23267–23275 (2017)
20. J.Y. Cho, X. Shi, J.R. Salvador, G.P. Meisner, J. Yang, H. Wang, A.A. Wereszczak, X. Zhou, C. Uher, Phys. Rev. B **84**(8), 085207 (2011)
21. Y. Li, G. Liu, T. Cao, L.M. Liu, J. Li, K. Chen, L. Li, Y. Han, M. Zhou, Adv. Funct. Mater. **26**(33), 6025–6032 (2016)
22. K. Chen, B. Du, N. Bonini, C. Weber, H. Yan, M. Reece, J. Phys. Chem. C **120**(48), 27135–27140 (2016)
23. Y. Liu, G. García, S. Ortega, D. Cadavid, P. Palacios, J. Lu, M. Ibáñez, L. Xi, J. De Roo, A.M. López, S. Martí-Sánchez, I. Cabezas, M. Mata, Z. Luo, C. Dun, O. Dobrozhan, D.L. Carroll, W. Zhang, J. Martins, M.V. Kovalenko, J. Arbiol, G. Noriega, J. Song, P. Wahnón, A. Cabot, J. Mater. Chem. A **5**(6), 2592–2602 (2017)
24. C. Xiao, K. Li, J. Zhang, W. Tong, Y. Liu, Z. Li, P. Huang, B. Pan, H. Su, Y. Xie, Mater. Horiz. **1**(1), 81–86 (2014)
25. M. Liu, F. Huang, L. Chen, I. Chen, Appl. Phys. Lett. **94**(20), 202103 (2009)
26. W.G. Zeier, A. Lalonde, Z.M. Gibbs, C.P. Heinrich, M. Panthofer, G.J. Snyder, W. Tremel, J. Am. Chem. Soc. **134**(16), 7147–7154 (2013)
27. M.L. Liu, I.W. Chen, F.Q. Huang, L.D. Chen, Adv. Mater. **21**(37), 3808–3812 (2009)
28. Q. Song, P. Qiu, F. Hao, K. Zhao, T. Zhang, D. Ren, X. Shi, L. Chen, Adv. Electron Mater. **2**(12), 1600312 (2016)
29. D. Zhang, J. Yang, Q. Jiang, Z. Zhou, X. Li, J. Xin, A. Basit, Y. Ren, X. He, Nano Energy **36**, 156–165 (2017)
30. H. Cabrera, I. Zumeta Dub, D. Korte, P. Grima Gallardo, F. Alvarado, J. Aitken, J.A. Brant, J.H. Zhang, A. Caldern, E. Marn, M. Aguilar Frutis, J.E. Erazo, E. Perez Cappe, M. Franko, J. Alloys Compd. **651**, 490–496 (2015)
31. Y. Pei, G. Tan, D. Feng, L. Zheng, Q. Tan, X. Xie, S. Gong, Y. Chen, J. Li, J. He, M. Kanatzidis, L. Zhao, Adv. Energy Mater. **7**(3), 1601299 (2017)
32. J.L. Cui, Y.Y. Li, Y. Deng, Q.S. Meng, Y.L. Gao, H. Zhou, Y.P. Li, Intermetallics **31**, 217–224 (2012)
33. L. Xi, Y.B. Zhang, X.Y. Shi, J. Yang, X. Shi, L.D. Chen, W. Zhang, J. Yang, D.J. Singh, Phys. Rev. B **86**(15), 155201 (2012)
34. H. Liu, X. Shi, F. Xu, L. Zhang, W. Zhang, L. Chen, Q. Li, C. Uher, T. Day, G.F. Snyder, Nat. Mater. **11**(5), 422 (2012)
35. L. Pan, D. Berardan, N. Dragoe, J. Am. Chem. Soc. **135**(13), 4914–4917 (2013)
36. K. Samanta, N. Gupta, H. Kaur, L. Sharma, S. Dogra Pandey, J. Singh, T.D. Senguttuvan, N. Dilawar Sharma, A.K. Bandyopadhyay, Mater. Chem. Phys. **151**, 99–104 (2015)
37. C. Rincon, Solid State Commun. **64**(5), 663–665 (1987)
38. S.H. Wei, L.G. Ferreira, A. Zunger, Phys. Rev. B **45**(5), 2533 (1992)
39. M.T. Ng, C.B. Boothroyd, J.J. Vittal, J. Am. Chem. Soc. **128**(22), 7118–7119 (2006)
40. Y.X. Qi, Q.C. Liu, K.B. Tang, Z.H. Liang, Z.B. Ren, X.M. Liu, J. Phys. Chem. C **113**(10), 3939–3944 (2009)
41. J. Fan, W. Carrillo-Cabrera, L. Akselrud, I. Antonyshyn, L. Chen, Y. Grin, Inorg. Chem. **52**(19), 11067–11074 (2013)
42. M. Siyar, J.Y. Cho, Y. Youn, S. Han, M. Kim, S.H. Bae, C. Park, J. Mater. Chem. C **6**(7), 1780–1788 (2018)

43. M. Ibáñez, R. Zamani, W. Li, D. Cadavid, S. Gorsse, N.A. Katcho, A. Shavel, A.M. López, J.R. Morante, J. Arbiol, A. Cabot, Chem. Mater. **24**(23), 4615–4622 (2012)
44. Y. Shen, C. Li, R. Huang, R. Tian, Y. Ye, L. Pan, K. Koumoto, R. Zhang, C. Wan, Y. Wang, Sci. Rep. **6**, 32501 (2016)
45. K. Yu, E.A. Carter, Chem. Mater. **28**(3), 864–869 (2016)
46. S. Schorr, G. Gonzalez Aviles, Phys. Stat. Solid A **206**(5), 1054–1058 (2009)
47. S. Nakamura, T. Maeda, T. Wada, Jpn. J. Appl. Phys. **49**(12R), 121203 (2010)
48. J.J.S. Scragg, L. Choubrac, A. Lafond, T. Ericson, C. Platzer-Björkman, Appl. Phys. Lett. **104** (4), 041911 (2014)
49. T. Gürel, C. Sevik, T. Çağın, Phys. Rev. B **84**(20), 205201 (2011)
50. S. Schorr, Sol. Energy Mater. Sol. Cells **95**(6), 1482–1488 (2011)
51. R. Djemour, M. Mousel, A. Redinger, L. Gütay, A. Crossay, D. Colombara, P. Dale, S. Siebentritt, Appl. Phys. Lett. **102**(22), 222108 (2013)
52. S. Chen, A. Walsh, X.G. Gong, S.H. Wei, Adv. Mater. **25**(11), 1522–1539 (2013)
53. Y.B. Zhang, L.L. Xi, Y.W. Wang, J.W. Zhang, P.H. Zhang, W.Q. Zhang, Comput. Mater. Sci. **108**, 239–249 (2015)
54. J. Yang, L. Xi, W. Qiu, L. Wu, X. Shi, L. Chen, J. Yang, W. Zhang, C. Uher, D. Singh, NPG Comput. Mater. **2**, 15015 (2016)
55. H. Shao, X. Tan, T. Hu, G.-Q. Liu, J. Jiang, H. Jiang, EPL Europhys. Lett. **109**(4), 47004 (2015)
56. Y. Zhang, E. Skoug, J. Cain, V. Ozoliņš, D. Morelli, C. Wolverton, Phys. Rev. B **85**(5), 054306 (2012)
57. D. Zhang, H.C. Bai, Z.L. Li, J.L. Wang, G.S. Fu, S.F. Wang, Chin. Phys. B **27**(4), 047206 (2018)
58. J. Zhang, R. Liu, N. Cheng, Y. Zhang, J. Yang, C. Uher, X. Shi, L. Chen, W. Zhang, Adv. Mater. **26**(23), 3848–3853 (2014)
59. W.G. Zeier, H. Zhu, Z.M. Gibbs, G. Ceder, W. Tremel, G.J. Snyder, J. Mater. Chem. C **2**(47), 10189–10194 (2014)
60. D. Zhang, J. Yang, Q. Jiang, Z. Zhou, X. Li, J. Xin, A. Basit, Y. Ren, X. He, W. Chu, J. Hou, ACS Appl. Mater. Interfaces **9**(34), 28558–28565 (2017)
61. P. Limelette, S. Hébert, V. Hardy, R. Frésard, C. Simon, A. Maignan, Phys. Rev. Lett. **97**(4), 046601 (2006)
62. J. Yao, N.J. Takas, M.L. Schliefert, D.S. Paprocki, P.E.R. Blanchard, H. Gou, A. Mar, C.L. Exstrom, S.A. Darveau, P.F.P. Poudeu, J.A. Aitken, Phys. Rev. B **84**(7), 075203 (2011)
63. Y.F. Ye, Q. Wang, J. Lu, C.T. Liu, Y. Yang, Mater. Today **19**(6), 349–362 (2016)
64. R.H. Liu, H.Y. Chen, K.P. Zhao, Y.T. Qin, B.B. Jiang, T.S. Zhang, G. Sha, X. Shi, C. Uher, W.Q. Zhang, L.D. Chen, Adv. Mater. **29**(38), 1702712 (2017)
65. S. Shafeie, S. Guo, Q. Hu, H. Fahlquist, P. Erhart, A. Palmqvist, J. Appl. Phys. **118**(18), 184905 (2015)
66. X.Y. Zhou, G.W. Wang, L.J. Guo, H. Chi, G.Y. Wang, Q.F. Zhang, C.Q. Chen, T. Thompson, J. Sakamoto, V.P. Dravid, G.Z. Cao, C. Uher, J. Mater. Chem. A **2**(48), 20629–20635 (2014)
67. Y.B. Luo, J.Y. Yang, Q.H. Jiang, Y. Xiao, L.W. Fu, W.X. Li, D. Zhang, Z.W. Zhou, Y.D. Cheng, Nano Energy **18**, 37–46 (2015)
68. W. Li, Y. Luo, Y. Zheng, C. Du, Q. Liang, B. Zhu, L. Zhao, J. Mater. Sci. Mater. El **29**(6), 4732–4737 (2017)
69. Y. He, P. Lu, X. Shi, F.F. Xu, T.S. Zhang, G.J. Snyder, C. Uher, L.D. Chen, Adv. Mater. **27** (24), 3639–3644 (2015)
70. C. Li, Y. Shen, R. Huang, A. Kumamoto, S. Chen, C. Dai, M. Yoshiya, S. Fujii, K. Funai, C.A.J. Fisher, Y. Wang, R. Qi, C.G. Duan, L. Pan, J. Chu, T. Hirayama, Y. Ikuhara, ACS Appl. Nano Mater. **1**(6), 2579–2588 (2018)
71. P.A. Zong, R. Hanus, M. Dylla, Y. Tang, J. Liao, Q. Zhang, G.J. Snyder, L. Chen, Energy Environ. Sci. **10**, 183–191 (2017)
72. X. Hu, P. Jood, M. Ohta, M. Kunii, K. Nagase, H. Nishiate, M.G. Kanatzidis, A. Yamamoto, Energy Environ. Sci. **9**(2), 517–529 (2016)

73. E.J. Skoug, J.D. Cain, D.T. Morelli, J. Electron. Mater. **41**, 1232–1236 (2012)
74. D. Chen, Y. Zhao, Y. Chen, B. Wang, Y. Wang, J. Zhou, Z. Liang, ACS Appl. Mater. Interfaces **7**, 24403–24408 (2015)
75. Y. Fujii, A. Kosuga, J. Electron. Mater. **47**(6), 3105–3112 (2018)
76. A. Kosuga, Y. Fujii, Rare Metals **37**(4), 360–368 (2018)
77. T. Barbier, P. Lemoine, S. Gascoin, O. Lebedev, A. Kaltzoglou, P. Vaqueiro, A. Powell, R. Smith, E. Guilmeau, J. Alloys Compd. **634**, 253–262 (2015)
78. H. Tang, F.H. Sun, J.F. Dong, H.L. Zhuang, Y. Pan, J.F. Li, Nano Energy **49**, 267–273 (2018)
79. M.T. Barako, W. Park, A.M. Marconnet, M. Asheghi, K.E. Goodson, J. Electron. Mater. **42**, 372–381 (2013)
80. K. Tyagi, B. Gahtori, S. Bathula, V. Toutam, S. Sharma, N.K. Singh, A. Dhar, Appl. Phys. Lett. **105**, 261902 (2014)
81. G. Li, Q. An, S.I. Morozov, B. Duan, P. Zhai, Q. Zhang, W.A. Goddard, G.J. Snyder, J. Mater. Chem. A **6**, 11743–11750 (2018)
82. G. Li, U. Aydenir, B. Duan, M.T. Agne, H. Wang, M. Wood, Q. Zhang, P. Zhai, W.A. Goddard, G.J. Snyder, ACS Appl. Mater. Interfaces **9**(46), 40488–40496 (2017)
83. Y. Zheng, Q. Zhang, X.L. Su, H.Y. Xie, S.C. Shu, T.L. Chen, G.J. Tan, Y.G. Yan, X.F. Tang, C. Uher, G.J. Snyder, Adv. Energy Mater. **5**, 1401391 (2015)
84. K. Yin, X. Su, Y. Yan, H. Tang, M.G. Kanatzidis, C. Uher, X. Tang, Scr. Mater. **126**, 1–5 (2017)
85. Z. Chen, Z. Jian, W. Li, Y. Chang, B. Ge, R. Hanus, J. Yang, Y. Chen, M. Huang, G.J. Snyder, Y. Pei, Adv. Mater. **29**, 1606768 (2017)
86. Q. Zhang, B. Liao, Y. Lan, K. Lukas, W. Liu, K. Esfarjani, C. Opeil, D. Broido, G. Chen, Z. Ren, Proc. Natl. Acad. Sci. **110**(33), 13261–13266 (2013)
87. H. Yang, J.H. Bahk, T. Day, A.M.S. Mohammed, G.J. Snyder, A. Shakouri, Y. Wu, Nano Lett. **15**(2), 1349–1355 (2015)
88. W. Liu, Q. Jie, H.S. Kim, Z. Ren, Acta Mater. **87**, 357–376 (2015)
89. N. Wang, L. Han, H. He, N.H. Park, K. Koumoto, Energy Environ. Sci. **4**(9), 3676–3679 (2011)
90. P. Huen, W.A. Daoud, Renew. Sust. Energ. Rev. **72**, 1295–1302 (2017)